Design of a 400 kV deep underground, high detector efficiency, high target density, high beam intensity accelerator facility

A. Lemut,[1,*] M. Couder,[2] D. Winklehner,[3] U. Greife,[4] A. Hodgkinson,[1] D. Leitner,[3] M. Leitner,[3] J. S. Saba,[1] P. A. Vetter,[1] W. L. Waldron,[1] and M. Wiescher[2]

[1]*Lawrence Berkeley National Laboratory, Berkeley, California 94720, USA*
[2]*University of Notre Dame, Notre Dame, Indiana 46556, USA*
[3]*Michigan State University, East Lansing, Michigan 48824, USA*
[4]*Colorado School of Mines, Golden, Colorado 80401, USA*

(Received 25 July 2011; published 4 October 2011)

Thermonuclear reaction cross sections of astrophysical interest decrease exponentially with energy, approaching the level of femtobarn or less at the Gamow window. Experimental investigations of such small reaction rates in laboratories at the earth's surface are hampered by the cosmic-ray background into detectors. For such studies, Dakota Ion Accelerator for Nuclear Astrophysics, a deep underground, high detector efficiency, high target density, high beam intensity accelerator facility is being designed. We report on a 100 mA, 400 kV accelerator design. To take into account the beam space-charge effects, advanced three-dimensional transportation calculations have been performed. These highly realistic beam calculations demonstrate that high beam currents can be transported to a gas-jet target with a diameter of few millimeters.

DOI: 10.1103/PhysRevSTAB.14.100101 PACS numbers: 29.20.Ba, 29.25.Ni, 29.27.Ac, 29.27.Eg

I. INTRODUCTION

Current stellar model simulations are at a level of precision such that nuclear reaction rates represent a major source of uncertainty for theoretical predictions of energy production and nucleosynthesis in stars and the analysis of the associated observational signatures. To address several open questions in cosmology, astrophysics, and neutrino physics, new high-precision measurements of direct-capture nuclear fusion cross sections will be essential [1–3]. At low energies, the nonresonant reaction cross section $\sigma(E)$ drops down almost exponentially with decreasing energy E because of the tunneling probability through the Coulomb barrier [4]. The Maxwellian-averaged reaction rate in a star depends critically on the reaction cross section [5]. The extremely low values of $\sigma(E)$ at the stellar energy range prevent its measurement in a laboratory at the earth's surface. The signal-to-noise ratio is too small, even with the highest beam intensities presently available from industrial accelerators, because of cosmic-ray interactions with the detectors.

One solution is to install an accelerator facility deep underground where the cosmic-ray background into detectors is reduced by several orders of magnitude [6,7]. This has been clearly demonstrated at the Laboratory for Underground Nuclear Astrophysics (LUNA) by the successful studies of critical reactions in the pp chains and first reaction studies in the CNO cycles [8,9]. However, many critical reactions still need high-precision measurements [1], and a next generation facility, capable of very high beam currents over a wide energy range with state-of-the-art target and detection technology, is highly desirable. The Dakota Ion Accelerator for Nuclear Astrophysics (DIANA) facility is being designed to face the low laboratory reaction rates near the stellar energy range by delivering high ion beam currents to a high density, supersonic gas-jet target, as well as to solid-target stations. In particular, three fundamental scientific issues in stellar nucleosynthesis will be addressed by DIANA: (i) solar neutrino sources and the metallicity of the sun, (ii) carbon-based nucleosynthesis, and (iii) neutron sources for the production of elements heavier than Fe in stars.

II. OVERVIEW OF THE DIANA ACCELERATOR FACILITY

The DIANA accelerator facility will consist of two accelerators: 50–400 kV and 0.4–3 MV (Fig. 1). Independent solid and gas-jet target stations are under design for both accelerators for conducting two experimental campaigns simultaneously (Fig. 1). This feature will greatly enhance the ability to carry out the planned science program, since the interchange of experimental setups is time consuming. The high-energy accelerator will have the capability to provide beam to the low-energy target stations (Fig. 1). This will allow a particular reaction to be measured with both accelerators in complementary energy

*ALemut@lbl.gov

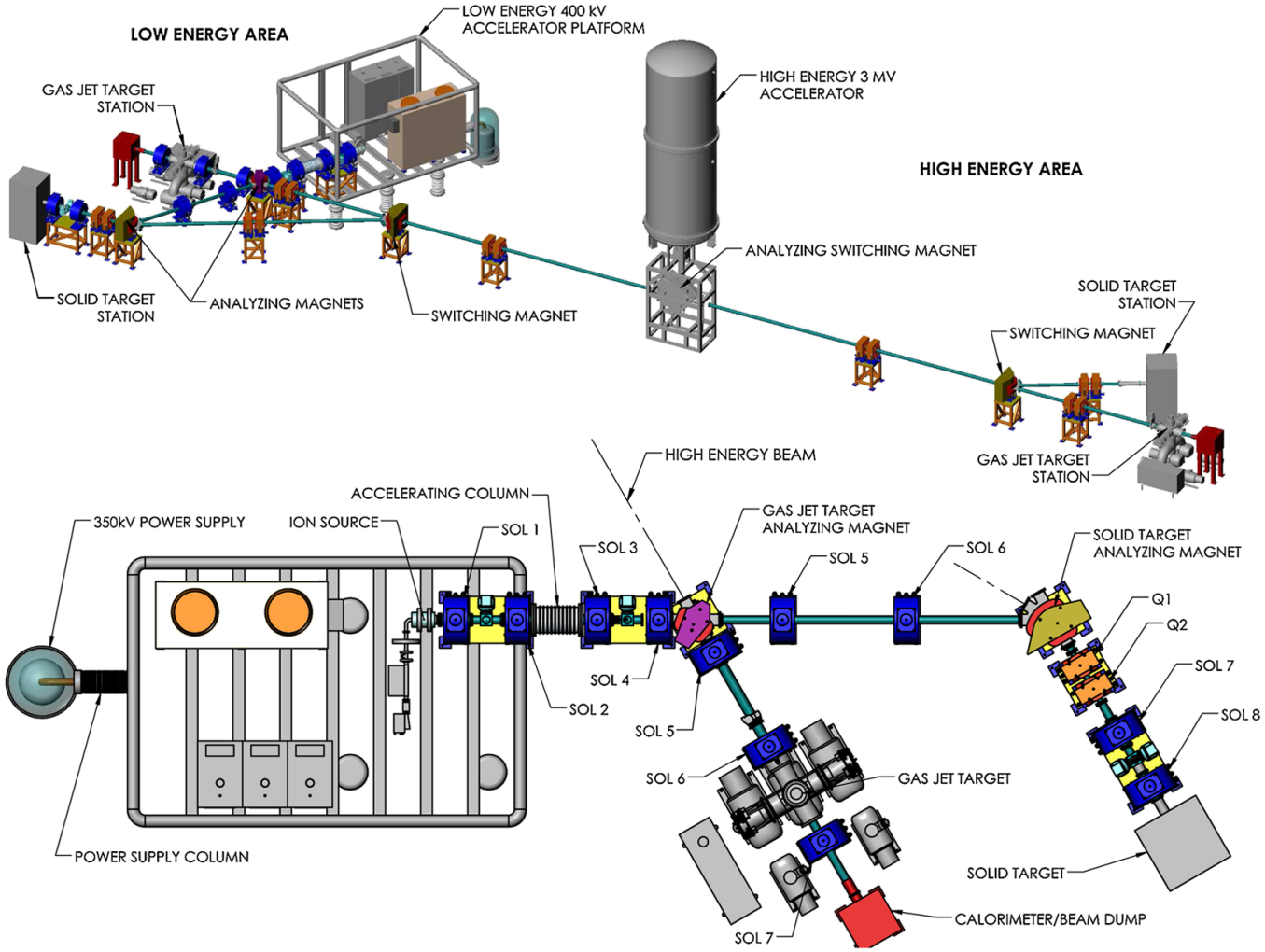

FIG. 1. Top: View of the DIANA accelerator facility. Bottom: The 400 kV accelerator, gas-jet, and solid-target stations layout.

ranges with identical target and detector setups, providing consistent high-precision data over a wide energy range. The DIANA high-energy accelerator facility, gas-jet target, and detectors will be presented elsewhere.

III. THE DIANA 400 KV ACCELERATOR

Measurements near the astrophysical energy range generate very low count rates (few counts/month to few counts/day [8,9]) and so require very intense ion beams and very long bombardment times (weeks to months). In the majority of low-energy accelerator designs, the ion source is directly coupled to the accelerator column. This is an economic solution, but unfortunately the beam current declines at low accelerating potentials. Therefore we adopted the open-air platform technique, where the ion source is completely decoupled from the accelerating potential (Fig. 1). All the beams are extracted at 50 kV ($^1H^+$ up to 100 mA and $^4He^+$ up to 50 mA, Sec. III A) and then postaccelerated up to 400 kV. This will allow for maximum optimization of the ion source parameters during tuning operations. Space-charge repulsion in such low-energy, high-current beams presents a difficult challenge for beam transport. The beam grows rapidly over short distances and requires closely spaced focal elements (Sec. III B). Target stations must be designed to withstand up to 5 kW of beam power in the case of a 100 mA beam of $^1H^+$ at 50 keV. To avoid excessive heating, the beam intensity will be scaled down while increasing the beam energy, to never exceed 5.0 kW. The experiments that will be performed at the DIANA 400 kV accelerator will require both solid and gas targets. Implanted solid targets have been engineered to withstand high beam powers, but at significant expense in cost and operational difficulty [10]. A similar device can also be used for evaporated or sputtered solid targets. For this reason, in the first phase of DIANA 400 kV operations, the solid-target station will be limited at 50 kV to 10 mA of $^1H^+$ (500 W) and 5 mA of $^4He^+$ (250 W), and the beam intensity will be scaled down accordingly while increasing the beam energy.

Beam heating in extended gas targets causes problematic local gas density reduction [11,12]. Supersonic gas-jet targets, with their high, continuous, fast gas flux, can withstand high beam power, making them a good choice for high-current beams [13]. For maximum experimental flexibility, the accelerator (Sec. III C, Fig. 1) is coupled to both supersonic gas-jet target (Sec. III D) and to solid-target stations (Sec. III E). Since astrophysically relevant cross sections decrease exponentially with energy, very narrow beam energy resolution is required: better than 10^{-3}, and ideally in the range of 2×10^{-4}. To minimize beam energy degradation, the gas-jet target will be windowless.

A. Ion source

Since their successful inception at the Chalk River laboratory, simple electron cyclotron resonance (ECR) ion sources have been proved to be capable of very high beam currents [14]. These ion sources require very little maintenance and are stable for long periods of time and are thus well suited to the long bombardments necessary at astrophysically relevant energies. The ion source design being considered is based on the recent developments on SIHLI at CEA/SACLAY [15]. The plasma chamber is 10 cm long and 5 cm radius. Aluminum has been chosen because of its favorable secondary electron emission properties and its resistance to plasma etching. Two solenoid coils will produce the 875 G axial magnetic field required to form and maintain the source plasma. A 1 kW, 2.45 GHz magnetron is coupled to the plasma chamber through a high-voltage window break and a ridged transition waveguide [15]. The ridges also concentrate the electric field at the center of the plasma chamber and redistribute the thermal load on the seal. A similar high-voltage break will be used for the gas inlet and a high-precision pressure gauge. All of the active elements are thus at the potential of the high-voltage platform. To prevent neutral gas pressure fluctuations, a feedback controller connected to the chamber pressure gauge will regulate the gas inflow. Only metal vacuum seals are used in the ion source and beam line to ensure the cleanest vacuum conditions. The extraction system consists of a tetrode electrode device (Fig. 2). The electrode design has been optimized to extract $^1H^+$ up to 100 mA and $^4He^+$ up to 50 mA. The extraction radius (4.5 mm) has been kept as low as possible to reduce the pumping speed requirements at the first pumping stage. A closely located puller electrode allows optimizing the shape of the plasma meniscus for high-current extraction. To allow for full beam optimization, independent power supplies are planned for the extraction, puller, and screening electrodes. The screening and ground electrode will be movable to allow optimization of the ion source. Particle phase space data calculated by the IGUN code [16] with the preliminary geometry shown in Fig. 2 are used as initial conditions for the three-dimensional beam calculations presented below.

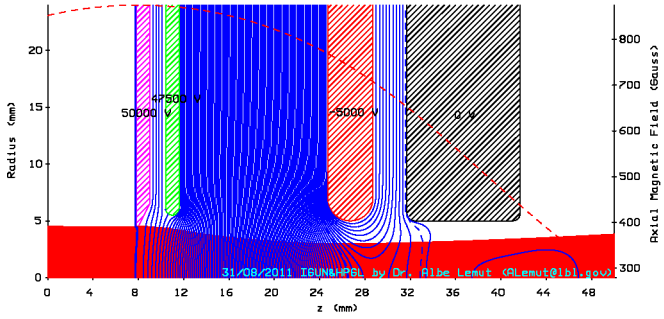

FIG. 2. Calculation of the extraction of $^4He^+$ 50 mA by means of the IGUN program [16]. The extraction electrode (shaded magenta area, inner radius 4.5 mm), the puller electrode (shaded green area), screening electrode (shaded red area), ground electrode (shaded black area), particle trajectories (red), and equipotential lines (blue) for a 50 kV extraction voltage are shown. The final ($z = 50$ mm) beam emittance $\epsilon_{4\,\mathrm{rms}}$ is 4π mm mrad, the radius 3.9 mm, and the divergence 55.1 mrad. The axial magnetic field (dashed red line), and the -200 V equipotential (dashed blue lines) are also plotted (see text in Sec. III B).

B. Transportation of low-energy high current beams

A high-current, low-energy beam expands rapidly due to space-charge repulsion, which complicates beam transport [17]. For a uniform density, round and parallel beam, the potential difference ΔV between the center and the beam envelope due to the space charge is

$$\Delta V = \frac{I}{4\pi\epsilon_0}\sqrt{\frac{m_{\mathrm{ion}}}{2E_{\mathrm{ion}}}}, \tag{1}$$

where I is the ion beam electrical current, m_{ion} the ion mass, and E_{ion} is the ion laboratory kinetic energy. For a 100 mA, 50 keV $^1H^+$ and 50 mA $^4He^+$ beam, $\Delta V =$ 289.4 V. These large potential differences generate considerable beam growth over short distances. Trapped low-energy electrons produced by ionization of residual gas in the pressure range of 10^{-6}–10^{-3} mbar can significantly reduce the ion beam space charge [17]. The slow positive ions created are repelled outside the beam envelope. As soon as an equilibrium is reached (usually in a few μs) between the electrons, the positive ions, and the beam potential, the electron space charge will significantly neutralize the beam space charge. In a study by Holmes, the neutralization level was found to be 99% when the residual gas pressure was in the range of 10^{-4} mbar [17]. A recent study by Ferdinand *et al.* showed that, for a 75 keV, 130 mA $^1H^+$ beam, the neutralization level ranged from 95% to 99% when the residual gas pressure was in the range of 10^{-5} mbar [18]. In this study the experimental data were compared with a theoretical model by Soloshenko [19] showing good agreement. Therefore we estimated the neutralized beam potential ΔV_n using this

model. For $^1H^+$ 50 keV, 100 mA beam $\Delta V_n = 6.3$ V, and for $^4He^+$ 50 keV, 50 mA $\Delta V_n = 16.9$ V, corresponding to neutralization levels $f = 1 - \Delta V_n/\Delta V$ of 97.8% and 94.2%, respectively (residual gas pressure 10^{-5} mbar). However, if the residual gas pressure is reduced to 10^{-6} mbar, ΔV_n gets 26.6 V for $^1H^+$ 50 keV, 100 mA, and ΔV_n gets 53.3 V for $^4He^+$ 50 keV, 50 mA, decreasing the neutralization level to 90.8% and 81.6%, respectively. Therefore we plan to install devices to keep the residual gas pressure under control and as close as possible to the design figure of 10^{-5} mbar. If the predicted neutralization level is found to be 80%, the maximum beam intensities that can be transported at 50 keV will be reduced to 50 and 25 mA for $^1H^+$ and $^4He^+$, respectively. On the contrary, if the neutralization level is found to be higher, as indicated by previous measurements, the adopted design has room to transport higher beam intensities. It should be noted that the neutralization level increases with increasing beam energy. In the discussion below and ion beam optics calculations, we conservatively assume a 90% neutralization level (residual gas pressure 10^{-5} mbar). Figure 3 shows the beam growth for a $^4He^+$ 50 keV initial 0.5 cm radius round beam for selected beam currents. Note that, for a $^1H^+$ (proton) beam at 50 keV for the same currents, the beam envelope has less growth, but is still not negligible. To meet the high-current requirement at low beam energy, the worst case of the $^4He^+$ 50 keV beam at 50 mA has been assumed. From Fig. 3, it is clear that strong focusing elements are needed over short distances. It is crucial to minimize the number of focal elements for design simplicity and cost. Figure 4 shows beam envelopes for several converging beams, illustrating the beam growth after an axis symmetric focal element. From the results shown in Figs. 3 and 4, it is clear that, in order to transport a 50 keV $^4He^+$ 50 mA beam, focusing elements cannot be spaced less than 0.6 m

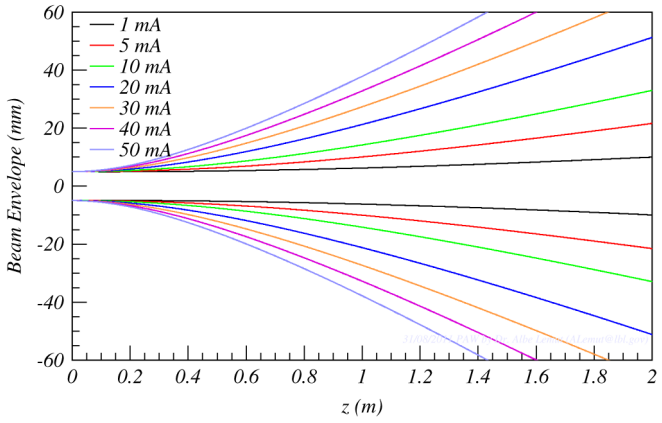

FIG. 3. Beam envelope growth for $^4He^+$ 50 keV initially quasiparallel ($\epsilon_{4\,\mathrm{rms}} = 4\pi$ mm mrad, beam envelope divergence 0.7 mrad), 0.5 cm radius, uniform, free drifting beams (neutralization 90%) at selected currents. The 50 mA beam reaches a 2 cm radius after 0.6 m.

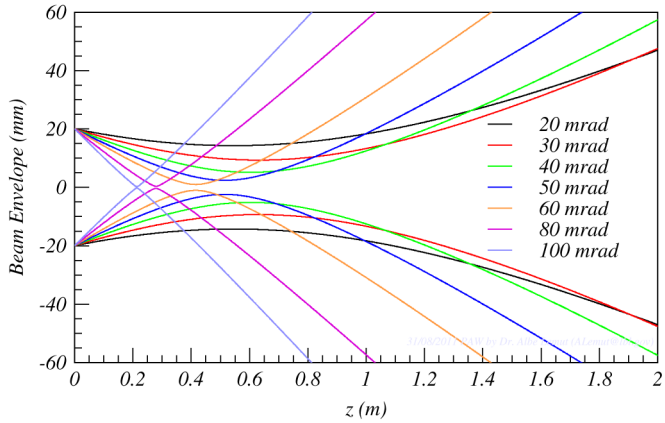

FIG. 4. $^4He^+$ 50 keV, 50 mA initially uniform (initial emittance $\epsilon_{4\,\mathrm{rms}} = 4\pi$ mm mrad), 2 cm radius, free drifting beams (neutralization 90%) for several initial converging angles. The longest drifting distance for the beam to reach the same initial radius is 1.3 m for the 30 mrad convergent beam.

and not more than 1.3 m. Solenoid lenses appear more suitable than quadrupole based elements to meet the short focusing requirements. Although magnetic quadrupole elements require less power (and cost) to operate than solenoids, quadrupoles' different vertical and horizontal focal lengths generate asymmetric beam envelopes which are very difficult to transport, particularly with the high space-charge beams. The solenoids also preserve beam roundness.

The beam envelopes shown in Figs. 3 and 4 were calculated using the WARP code, a three-dimensional (3D) particle-in-cell code [20]. Contrary to most classical matrix envelope calculators, for every step advance WARP calculates the space-charge field by means of its internal 3D electrostatic fields solver, and applies it to the particles. Furthermore, WARP can run calculations with more than one ion species at a time allowing calculation of space-charge effects for multiple-species ion beam transportation, in particular within the analyzing magnets. In addition, calculations performed with WARP can incorporate imported 3D magnetic field data to allow realistic trajectory calculations through designed magnetic elements. The WARP code can discard particles if their trajectories intersect beam pipes, slits, collimators, or any other user-defined surface. All of these WARP features have been extensively used in the results shown below for highly realistic beam optics calculations.

C. Accelerator layout

Figure 1 shows the 400 kV accelerator layout together with both gas-jet and solid-target stations. Figure 5 shows the results of a $^4He^+$ 50 keV, 50 mA beam optics calculation through the gas-jet target beam line. No particle losses are observed in this computation. The first solenoid lens after the ion source converts the strongly divergent

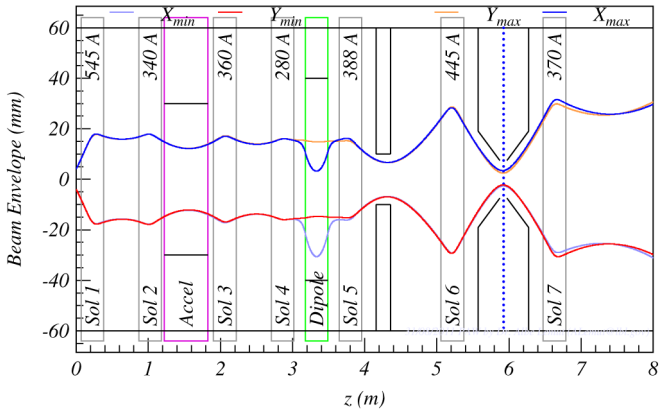

FIG. 5. $^4He^+$ 50 keV, 50 mA (2.5 kW, neutralization 90%, no postacceleration) beam envelopes through the gas-jet target station beam line. The dotted blue vertical line represents the gas-jet target location.

beam to nearly parallel to allow passage through the vacuum pumping stage (Figs. 1 and 5). To reduce the space-charge repulsion at low beam energies, large beam radii are necessary, so a 12 cm diameter pipe has been adopted. This way the beam will always pass through the uniform field region of the solenoids to minimize phase space aberrations. The solenoids' design has been optimized using the OPERA-3D/TOSCA magnetostatic code [21]. The solenoid axial peak field at the full excitation (1000 A) is 1.4 T, the effective field length is 0.19 m. Figure 6 shows the axial and radial components of the magnetic field. Three-dimensional magnetic maps have been calculated for several excitation currents and imported with linear current interpolation into the WARP code. This allows realistic accounting in beam transport for small field nonlinearities from B-field saturation in the yoke material. An emittance

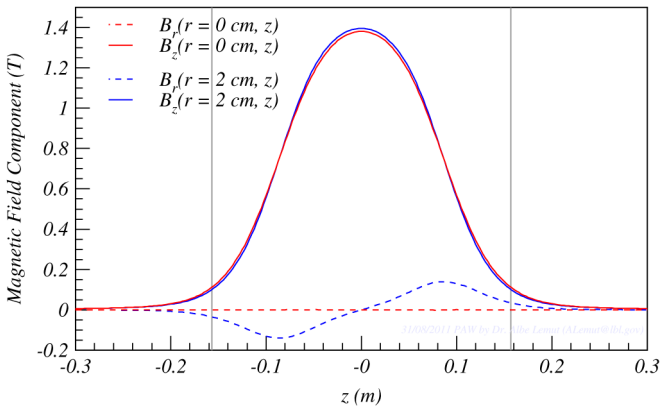

FIG. 6. Radial B_r (dashed lines) and axial B_z (solid lines) magnetic field components of the solenoid lenses calculated by OPERA-3D/TOSCA [21] for the center-line beam trajectory ($r = 0$ cm, red) and at radius $r = 2$ cm (blue). The vertical grey lines represent the yoke face to face extension of the lens.

scanner and an isolation valve will also be installed in the pumping stage.

The second solenoid lens matches the beam to the entrance of the 350 kV accelerator tube. A negative screen electrode prevents secondary electrons trapped near ground potential from being accelerated back into the column. When powered, there will be no space-charge neutralization inside the accelerator column, since the residual trapped electrons will be removed by the electric field. Therefore inside the column the beam radius will grow very rapidly, even at low beam currents (more than shown in Fig. 3), potentially scraping along the tube walls. This effect will be stronger at low accelerating voltages [Eq. (1)]. Thus, it is of primary importance to design the accelerator tube to be as short as possible to reduce the length where the beam space charge is not neutralized at all. However, with postacceleration voltages ranging from 0 to 350 kV, the optimal tube length will vary considerably with voltage. An alternative solution is to adopt a movable screening electrode inside the accelerator column (Fig. 7). The WARP 3D internal electric field solver has been used to calculate the field generated by the accelerating column and movable electrodes. Several conductor geometries have been studied, and the one we have adopted minimizes the region of full space charge for the beam at low accelerating voltages while maintaining high performances at higher voltages (see text below). For every accelerating voltage, a 3D electric field map is calculated by WARP, using the screening voltage and the required distance from high voltage to screening electrode.

At first order, the electrons trapped by the beam space charge reach an equilibrium where their velocity

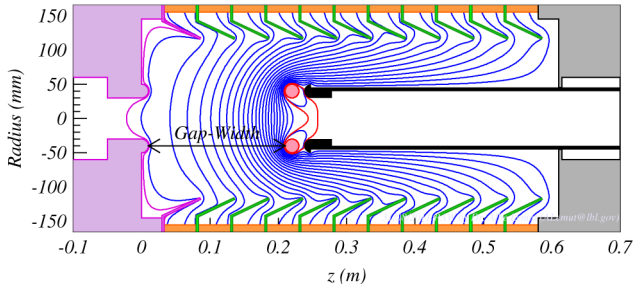

FIG. 7. Schematic of the accelerator column and movable screening electrode. The high-voltage electrode (magenta, on the left), the negative screening ring (red, electrically insulated), the movable ground tube ground (black), the ceramic insulators (orange), and the uniformly voltage graded accelerator rings are also shown (green). The first ring (magenta) is at platform potential. The equipotential lines for a 150 kV postacceleration voltage (200 mm gap width) are shown in blue. The −200 V (red) and 149.8 kV (magenta) equipotential lines indicate the area where the beam is transported with full space charge applied. In order to accommodate large beam radii, the acceleration electrode assembly has an inner radius of 30 mm.

distribution is Maxwellian, characterized by a temperature T. According to the study of Holmes, the trapped electron temperatures for 100 mA $^1H^+$ and 50 mA $^4He^+$ 50 keV beams are expected to be in the range of 40–100 eV for a residual gas pressure of 10^{-5} mbar [17]. Therefore, the screen electrode voltage is chosen to generate a minimum of at least −200 V along the beam axis (Fig. 8). We assume that in the region where the postaccelerating voltage is between (HV − 200 V) and −200 V (where HV is the postacceleration voltage), the beam is at full space charge. The two z points that fulfill this condition are determined by analyzing the potential map calculated by WARP. Figure 8 shows an example of this procedure, where the potential and electric field components are calculated for a postacceleration voltage of 2 kV. If voltages are considered along trajectories with different radii, small differences are observed in the region of full space charge. The longest region of full space charge is found on the trajectory along the center line; we use this trajectory in our calculations to be conservative.

It should be noted that when the screen electrode is at central positions the accelerating field is enhanced in the proximity of the movable electrode systems (Fig. 7). To compensate for this effect, the screen electrode potential should be lowered down to −8 kV. As a result, the region where the beam is at full space charge has a small increase. A possible solution to reduce this effect is to short the column. However, for postaccelerating voltages above 50–100 kV, the effect on beam expansion is small and is compensated by means of the solenoids. For postaccelerating voltages below 50–100 kV (gap widths below 37–125 mm), the length of the region where the beam is at full space charge is dominated by the extension of the fringe field (Fig. 8), and therefore shorting the column provides negligible improvement. The natural solution to reduce the fringe field extension is to adopt electrodes with small inner diameter, but at the expense of the maximum beam diameter.

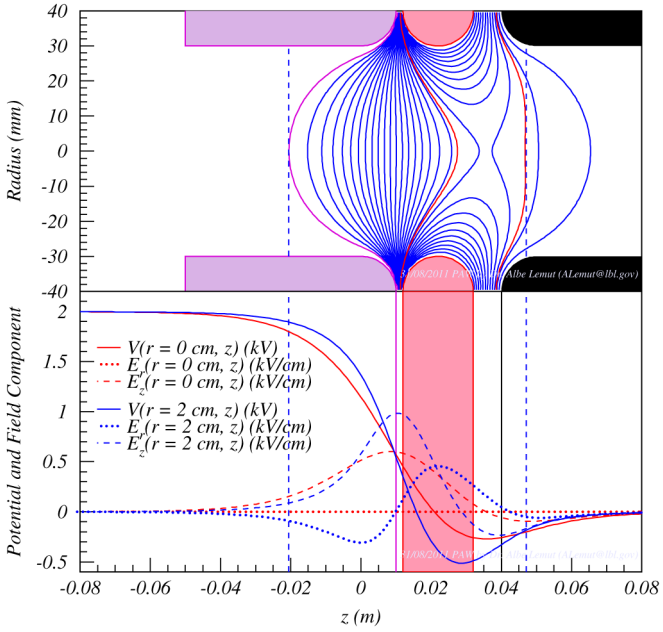

FIG. 8. Top: Potential for a 2 kV postacceleration voltage, −1.3 kV screening voltage, 2 mm gap width. Bottom: Voltage, for potential shown on top, along the center line (solid blue line) and radius 2 cm (solid red line) trajectories. The radial E_r (dotted lines) and axial E_z (dashed lines) electric field components are also shown. The magenta vertical line represents the high-voltage electrode tip, the red area the screen electrode extension, and the black vertical line the ground electrode tip (see top figure). The blue vertical lines represent the points where the axial voltage is 1.8 kV and −200 V. The space-charge length is 67.6 mm. The z coordinate is the same as Fig. 7.

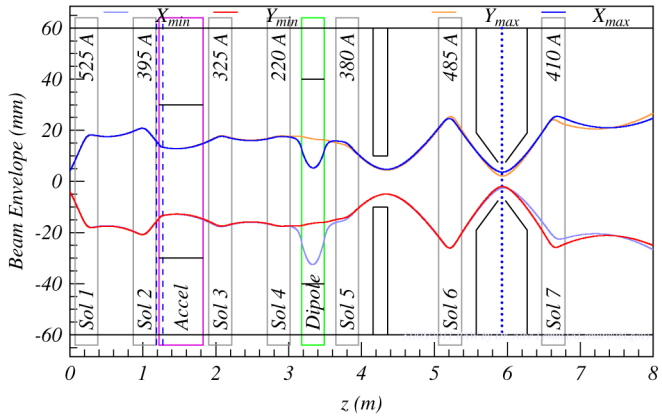

FIG. 9. $^4He^+$ 60 keV, 50 mA (10 kV postacceleration, 3 kW, gap width 2.6 mm, screening voltage −3 kV, neutralization 90%) beam envelopes through the gas-jet target station beam line. Between the two dashed blue vertical lines the beam is treated at full space charge (length 86.4 mm).

As an example, Fig. 9 shows the results of a 50 mA, 60 keV $^4He^+$ (10 kV postacceleration) calculation, for the gas-jet target beam line. The third lens after the column will match the beam to nearly parallel to pass through another pumping stage (Figs. 5 and 9), equipped with beam diagnostics. To improve the pumping through the movable ground tube (which will obstruct the pumping apertures when completely retracted), it will be gridded. A similar device will be adopted on the high-voltage flange.

The fourth solenoid lens will match the beam to enter the analyzing magnet (Figs. 5 and 9). This is designed to be a four-way-cross switching magnet. When powered, the dipole will bend the beam into the gas-jet target beam line.

D. Gas-jet target beam line

The gas-jet target analyzing magnet is a 60° dipole magnet with a bending radius of 30 cm. Since large beam radii are expected, the vertical gap is 8 cm high (± 4 cm from the center-line trajectory), while the horizontal is 12 cm wide (± 6 cm) to ensure a large region of

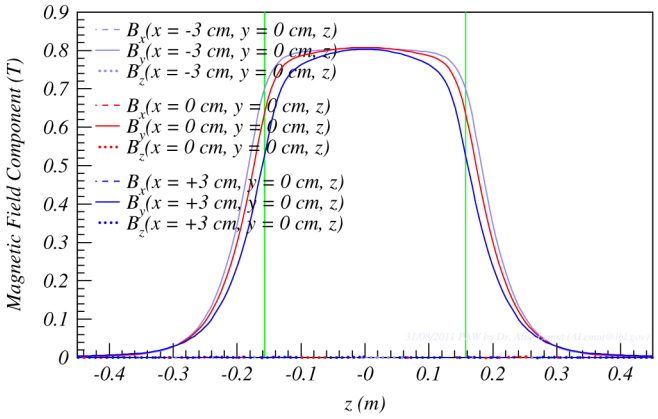

FIG. 10. B_x (dashed lines), B_y (solid lines), and B_z (dotted lines) components of the gas-jet target analyzing magnet calculated by OPERA-3D/TOSCA [21]. Three different trajectory are shown: inner ($x = -3$ cm, $y = 0$ cm, light blue), center line ($x = 0$ cm, $y = 0$ cm, red), and outer ($x = -3$ cm, $y = 0$ cm, blue). The B_x and B_z values are very close to zero, and therefore overlap with each other. The vertical green lines represent the magnet pole-face to pole-face extension along the center-line trajectory.

good magnetic field. This dipole has been designed using the OPERA-3D/TOSCA magnetostatic code [21]. To preserve the beam roundness, both entrance and exit pole-face angles are set to 20.8° to focus both vertical and horizontal planes into the same point. The field at full excitation (215 A) is 0.8 T. Figure 10 shows the Cartesian magnetic field components calculated by means of OPERA-3D/TOSCA. Magnetic maps have been calculated for several excitation currents. These calculations show that at these field strengths, negligible nonlinearities are expected into the yokes. We investigated the effects of dipole and solenoid fringe field interactions, finding no nonlinear interaction over the whole excitation current range, and in particular in the area where the beam will pass through. In any real magnet, the fringe fields (Fig. 10) will extend outside the ideal bending boundary. On the horizontal plane the beam therefore begins to bend inward (if the B_y field component is positive, otherwise outward) before actually entering the bending region (Figs. 5 and 9). Therefore the trajectory of the center of the beam will not pass on the center-line trajectory. This is a natural effect, but most matrix-based codes cannot calculate it numerically. Since fringe field effects in matrix codes are modeled by means of "thin lenses" at the entrance and at the exit, their results are reliable outside the magnet boundaries (especially where the space charge effects are negligible). For this reason the large horizontal dipole pole width of ±6 cm has been adopted. To accommodate beam powers up to 5 kW, the dipole beam chamber will be cooled with low conductivity water (LCW, inlet temperature 20 C).

The gas-jet target chamber and pumping stages must be incorporated into the beam-line optics to accommodate the large beam radii and the necessary close spacing of solenoid lenses. To reduce environmental radioactive backgrounds in the detectors, the gas-jet target and detector region will be surrounded with a high radio-purity lead and copper shield. The heavy shielding must fit within a maximum beam-line length of 1.1 m from solenoid lens face to next solenoid lens face. In order to transport high beam currents through the pumping apertures, their location has to be matched to the beam envelopes for zero current losses. For this reason a pumping stage aperture has been placed after the fifth solenoid, close to the analyzing magnet focal point (Figs. 5 and 9). The fifth solenoid's task is to focus low-energy beams through the pumping stage collimator. This collimator will be LCW cooled and electrically insulated to monitor the beam current during the beam tuning operations. Another pumping stage together with beam diagnostics equipment is located between lens five and lens six.

The analyzing magnet and the pumping stage collimator have been designed to work together to eliminate any beam impurities from the beam of interest. Figure 11 illustrates the analyzing magnet separating capability for multiple beam species. From Fig. 11, it is clear that no parasitic beam will be able to reach the target. Parasitic beams will be absorbed far away from the target shielding to reduce any detected background from nuclear reactions occurring on pipe or aperture surfaces.

The longer spacing between the fifth and sixth lenses is necessary for the sixth lens to focus the beam at the target location. In fact, from Fig. 4 it is clear that a larger initial radius is needed in order to focus the beam at 0.55 m from the solenoid face (half target spacing), with a radius of few

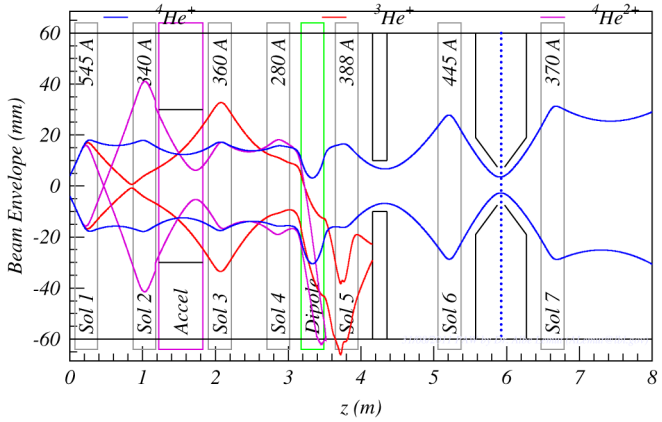

FIG. 11. Horizontal beam envelops for a $^4He^+$ 50 keV 50 mA, with 1 mA of $^3He^+$ and 1 mA $^4He^{2+}$ contaminations (neutralization 90%). While the $^4He^{2+}$ is eliminated in the analyzing magnet chamber, the $^3He^+$ is stopped by the pumping stage aperture. A similar study has been performed for a H^+ 50 keV 100 mA beam with 10 mA of H^{2+} and 1 mA of H^{3+}. In this case both parasitic beams are eliminated at the column entrance, by the analyzing magnet chamber and by the pumping stage aperture.

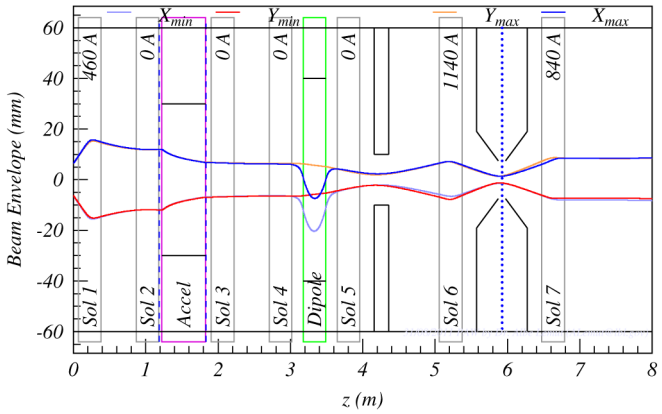

FIG. 12. $^4He^+$ 400 keV 12.5 mA (350 kV post acceleration, 5 kW, gap width 550 mm, screening voltage −5 kV, neutralization 90%) beam envelopes through the gas-jet target station beam line. Between the two dashed blue vertical lines (overlapped on the focal elements symbols), the beam is treated at full space charge (length 647.7 mm).

millimeters. Two conical collimators (LCW cooled, electrically insulated, 30 cm long, smaller radius 7.5 mm, larger radius 19 mm) will separate the target chamber pumping stage from the rest of the beam line. Each collimator will be located at ±5 cm from the gas-jet stream. The target collimator slope (38.3 mrad) has been optimized to match the beam envelopes and provide the required vacuum conductance.

The purpose of the seventh solenoid is to bring the beam down to the calorimeter (acting as a beam dump) for the beam current integration. To reduce possible beam-induced background, the calorimeter will also be enclosed in a lead shield.

Figure 12 shows the results of a 12.5 mA 400 keV $^4He^+$ (350 kV postacceleration voltage, 5 kW) beam calculation. Figure 12 shows that increasing the beam energy results in beam envelopes which are less sensitive to space-charge effects and conform more closely to classical matrix expectations.

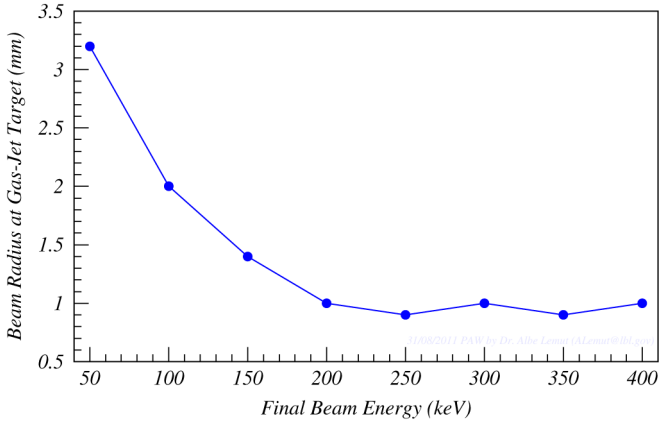

FIG. 13. $^4He^+$ beam radius at gas-jet target location for selected final beam energies. The beam current has been scaled down not to exceed 5 kW of beam power (neutralization 90%).

Figure 13 shows the beam radius calculated at the gas-jet target location for several $^4He^+$ final beam energies (the beam currents have been scaled down not to exceed 5 kW of beam power). Figure 13 demonstrates that beam diameters of a few mm can be achieved at the location of the gas-jet stream, which itself is being designed to have a diameter of 1 cm.

E. Solid-target beam line

The beam current to be delivered to the solid-target station is limited to 10 mA at 50 keV, corresponding to a beam power of 500 W. The fifth lens of the solid-target beam line will convert the diverging beam to nearly parallel trajectories, while the sixth will match the beam at the entrance of the solid-target dipole (Figs. 1 and 15). The solid target analyzing magnet is designed to be a three-way crossing. It can be operated to bend the beam from the 400 kV accelerator (60° bending angle) or the beam from the high-energy accelerator (30° bending angle) into the solid-target beam line. The low-energy bending radius is 0.38 m, while the high energy is 0.75 m. The low-energy entrance pole-face angle rotation is 30°, while the high energy is 15°. The exit pole face into the solid-target beam line is flat. Both the low- and high-energy beams have 4 cm vertical gap and 12 cm horizontal width (± 6 cm). The field at full excitation for the 60° bend is 0.6 T, while the field for the high energy is 1.7 T. This dipole has been designed using the OPERA-3D/TOSCA magnetostatic code [21]. Figure 14 shows the Cartesian magnetic field

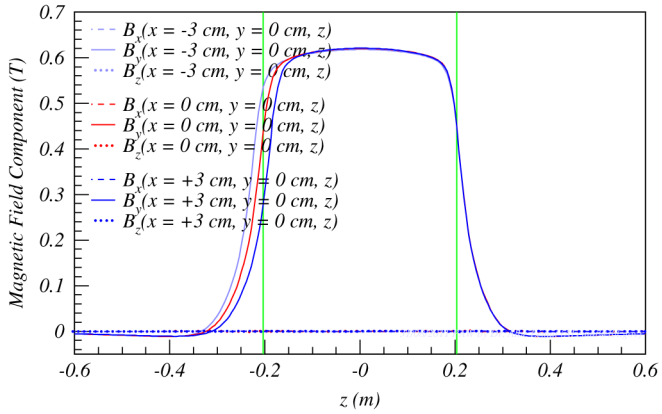

FIG. 14. B_x (dashed lines), B_y (solid lines), and B_z (dotted lines) components of the solid-target analyzing magnet calculated by OPERA-3D/TOSCA [21]. Three different trajectory are shown: inner ($x = -3$ cm, $y = 0$ cm, light blue), center line ($x = 0$ cm, $y = 0$ cm, red), and outer ($x = -3$ cm, $y = 0$ cm, blue). The B_x and B_z values are very close to zero, and therefore overlap with each other. The vertical green lines represent the magnet pole-face to pole-face extension along the center-line trajectory.

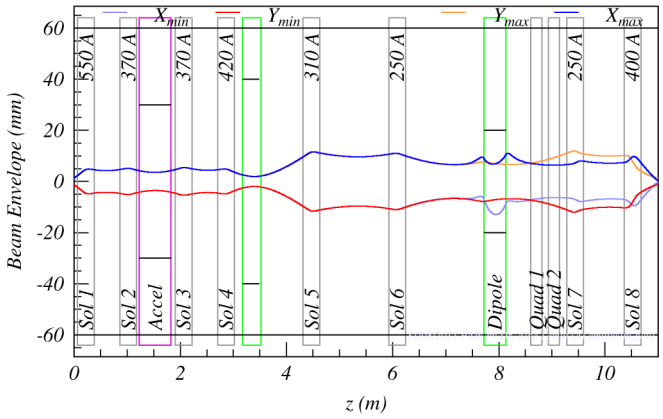

FIG. 15. $^4He^+$ 50 keV 5 mA (no postacceleration, 250 W, neutralization 90%) beam envelopes through the solid-target station beam line. The two high-energy quadrupoles are shown but not used in the present calculation.

components, calculated by means of OPERA-3D/TOSCA. Figure 15 shows the results of a 5 mA 50 keV $^4He^+$ (no postacceleration, 250 W) beam calculation. The seventh solenoid is designed to maintain the beam parallel until the eighth one which will focus the beam at the solid-target location. Similar to the gas-jet target dipole, on the horizontal plane the beam will start to bend before actually entering the bending region (Figs. 15 and 16). Because of the very close coil-to-pole design, the B_y fringe field component is negative (Fig. 14). Thus, the beam will start to bend outward before entering the dipole. Because of the 500 W beam power, the solid-target holder will be LCW cooled, and electrically insulated for current integration. Figure 16 shows the results of a 625 μA 400.0 keV $^4He^+$ (350 kV postacceleration, 250 W) beam calculation. The solid-target station will be embedded in a high radio-purity lead and copper shield. In this case, the space left after the eighth solenoid is sufficient to accommodate a shield.

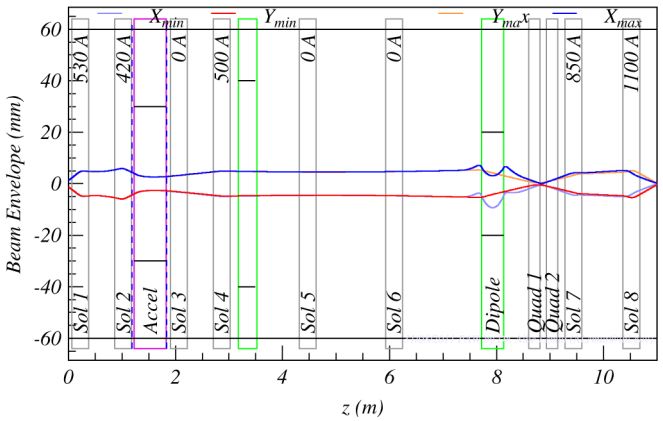

FIG. 16. $^4He^+$ 400 keV 625 μA (350 kV postacceleration, 250 W, neutralization 90%) beam envelopes through the solid-target station beam line. The two high-energy quadrupoles are shown but not used in the present calculation.

High-purity materials will be used in the construction of the target holder to prevent background from parasitic reactions. Although the beam radius at the solid target (radius 3 cm) is not as critical as in the gas-jet target beam-line design, beam radii of a few mm can be obtained (Figs. 15 and 16). In order to uniformly distribute the 500 W power across the active target surface (up to its maximum radius), electrostatic vertical and horizontal deflectors will be installed, and driven at low frequency (a few Hz) and low voltages (few 100 V). It should be noted that the effects on the reaction cross section determination due to the beam deflection on the target area are correct for by the detection efficiency measurements.

The effect of random misalignments up to 0.5 mm displacement from the center-line trajectory have been studied for both beam lines. It should be emphasized that, thanks to the large apertures of the focal elements, no beam losses have been found. The most sensitive elements are those solenoids followed by the longest drifting space in both the gas-jet and solid-target beam lines. The maximum displacement of the center line beam trajectory is found to be about 2 mm (in the solid-target beam line). Therefore the different elements of both beam lines will be aligned using a high-precision (75 μm) laser tracker system. In addition, steering coils (located after lens three and five for the gas-jet beam line, and before lens five and after lens six for the solid-target beam line) will be installed for correcting the residual misalignment during operations.

IV. CONCLUSIONS

The DIANA 400 kV accelerator facility has been designed to transport high beam currents to a gas-jet and a solid-target station. High currents of proton and helium beams, stable for long periods of time, can be provided by current generations of relatively simple ECR ion sources, making them a good choice for this facility. High beam intensity, low-energy accelerator design is challenging because of the rapid beam expansion caused by space-charge repulsion. An accelerator tube with a movable screen electrode has been designed to minimize the region where the beam is at full space charge. The solenoid focal elements and their spacing have been optimized to transport high beam currents, up to 100 mA of $^1H^+$ at 50 keV and up to 50 mA $^4He^+$ at 50 keV down to the gas-jet target station. Advanced three-dimensional beam transportation calculations show that beams with few millimeter radii can be achieved at both target stations.

ACKNOWLEDGMENTS

A. Lemut is deeply grateful to D. P. Grote of Lawrence Livermore National Laboratory for invaluable WARP support. This work is supported by the National Science Foundation NSF-09-500 grant, proposal ID 091728. This work was supported by the Director, Office of Science,

Office of Basic Energy Sciences, of the U.S. Department of Energy under Contract No. DE-AC02-05CH11231. This work was supported by the Assistant Secretary for Energy Efficiency and Renewable Energy, Office of Building Technology, State, and Community Programs, of the U.S. Department of Energy under Contract No. DE-AC02-05CH11231.

[1] E. G. Adelberger *et al.*, Rev. Mod. Phys. **83**, 195 (2011).
[2] T. A. Weaver and S. E. Woosley, Phys. Rep. **227**, 65 (1993).
[3] M. Busso, R. Gallino, and G. J. Wasserburg, Annu. Rev. Astron. Astrophys. **37**, 239 (1999).
[4] C. Rolfs and W. S. Rodney, *Cauldrons in the Cosmos* (University of Chicago Press, Chicago, 1988).
[5] C. Angulo *et al.*, Nucl. Phys. **A656**, 3 (1999).
[6] H. Costantini *et al.*, Rep. Prog. Phys. **72**, 086301 (2009).
[7] D. M. Mei and A. Hime, Phys. Rev. D **73**, 053004 (2006).
[8] M. Junker *et al.*, Phys. Rev. C **57**, 2700 (1998).
[9] A. Lemut *et al.*, Phys. Lett. B **634**, 483 (2006).
[10] M. Assuncão *et al.*, Phys. Rev. C **73**, 055801 (2006).
[11] J. Görres *et al.*, Nucl. Instrum. Methods **177**, 295 (1980).
[12] M. Marta *et al.*, Nucl. Instrum. Methods Phys. Res., Sect. A **569**, 727 (2006).
[13] J. Görres *et al.*, Nucl. Instrum. Methods Phys. Res., Sect. A **241**, 334 (1985).
[14] T. Taylor and J. S. C. Willis, Nucl. Instrum. Methods Phys. Res., Sect. A **309**, 37 (1991).
[15] R. Gobin *et al.*, in *Proceedings of the ECRIS 2008 Conference* (Argonne National Laboratory, Chicago, IL, 2008), p. MOPO-20.
[16] R. Becker and W. B. Herrmannsfeldt, Rev. Sci. Instrum. **63**, 2756 (1992).
[17] A. J. T. Holmes, Phys. Rev. A **19**, 389 (1979).
[18] R. Ferdinand *et al.*, in *Proceedings of the Particle Accelerator Conference, Vancouver, BC, Canada, 1997* (IEEE, New York, 1997), p. 2733.
[19] I. A. Soloshenko, Rev. Sci. Instrum. **67**, 1646 (1996).
[20] A. Friedman, D. P. Grote, and I. Haber, Phys. Fluids B **4**, 2203 (1992).
[21] Cobham plc, Brook Road, Wimborne, Dorset, BH21 2BJ, UK (http://www.cobham.com).